Low Vibration Design and Investigation of an Interior Permanent Magnet Motor in the Perspective of the Saliency Ratio

Hui Qu, Li Quan, Xiaoyong Zhu, *Member*, *IEEE*, Zixuan Xiang, Teng Liu, Jiamin Bai

***Abstract*—To address the issue of increased electromagnetic vibration in permanent magnet (PM) motors for electric vehicles under flux-weakening speed extension operation, this paper proposes a low-vibration design method for PM motors from the perspective of saliency ratio. First, by establishing a theoretical model for vibration analysis under flux-weakening operation, it reveals the vibration mechanism whereby high-order armature magnetomotive force (ARM-MMF) harmonics under flux-weakening operation leads to enhanced radial electromagnetic force (REF). Second, an in-depth investigation into the intrinsic relationship between saliency ratio and ARM-MMF is conducted. This study proposes a novel methodology to design key ARM-MMF harmonics that induce significant electromagnetic vibration from the perspective of the saliency ratio. An innovative rotor topology featuring elliptical-arc composite flux barriers is developed to implement this approach. Furthermore, and synergistic optimization is performed with the saliency ratio and torque as optimization objectives to balance vibration suppression and torque output performance. Finally, a prototype is manufactured and tested. Both theoretical and experimental analyses validated the effectiveness of the motor and the proposed design method.**

***Index Terms*—Permanent magnet (PM) motor, Armature magnetomotive force, Saliency ratio, Vibration suppression.**

I. Introduction

INTERIOR permanent magnet synchronous motors (IPMSMs) have gained widespread application in the electric vehicle sector due to their advantages of high power density and high efficiency [1]-[2]. Motor vibration, as one of the key indicators for evaluating motor performance, has always been a focal point of attention in both academic and industrial circles [3]-[4]. Compared with low-speed operation, electromagnetic vibration in electric vehicles significantly increases under flux-weakening speed extension, which not only affects ride comfort but also restricts further speed range extension. Research indicates that this exacerbation of vibration primarily stems from magnetic field distortion in the airgap caused by flux-weakening control [5]. While reducing the amplitude of fundamental waves to expand the speed range, this process generates higher-order spatial harmonic magnetic flux, thereby worsening electromagnetic vibration. Therefore, studying methods to suppress electromagnetic vibration in permanent magnet (PM) motors under flux-weakening operation hold significant importance.

Currently, in order to suppress vibrations caused by low-order radial electromagnetic force (REF), scholars have proposed numerous methods, such as using stator skew slots [6], rotor skew, and rotor slots in the motor structure itself [7]-[8], and injecting harmonic currents in control strategy optimization [9]. However, although these methods suppress electromagnetic vibrations, they inevitably compromise torque performance, and the complex manufacturing processes required for special structures increase manufacturing costs.

Generally speaking, from the perspective of vibration generation mechanisms, the armature magnetomotive force (ARM-MMF) is the primary source of excitation for electromagnetic vibration [10]. Therefore, some scholars have conducted a series of studies based on ARM-MMF. In [11], a star-delta hybrid winding structure has been proposed, which optimizes the superposition effect of the winding MMF by making the current phase angle and spatial phase angle of the delta winding behind the star winding by $\pi/2m$, where m is the phase number of the motor. This significantly weakens the amplitude of REF harmonics. In addition, a dual three-phase winding design is adopted in [12], with the two sets of windings spatially offset by 30° electrical angle. By leveraging the mutual cancellation effect of MMF within specific harmonic frequency bands, the excitation of REF harmonics is further reduced. Although these methods can suppress vibration while ensuring a certain torque output, they still have obvious limitations. On one hand, multi-phase winding systems increase control complexity and costs; on the other hand, existing solutions are mainly optimized for single rated operating conditions and fail to effectively address the issue of worsening electromagnetic vibration caused by enhanced armature reaction under flux-weakening operation.

Manuscript received July 20, 2025; revised September 23, and November 27, 2025; accepted December 12, 2025. Date of publication December 25, 2025; Date of current version December 19, 2025.

This work was supported in part by the Modern Agriculture Major Core Technology Innovation Project of Jiangsu Province under Grant CX(22)1005, and in part by the National Natural Science Foundation of China under Grant 52177046, and in part by the Project of Innovation of Postgraduate of Jiangsu Province under Grant KYCX25_4228.

Hui Qu, Li Quan, Xiaoyong Zhu, Zixuan Xiang, Teng Liu, and Jiamin Bai are with Jiangsu University, Zhenjiang 212013, China (2222307034@stmail.ujs.edu.cn; quanli@ujs.edu.cn; zxyff@ujs.edu.cn; zxxiang@ujs.edu.cn; 2112307122@stmail.ujs.edu.cn; 2112307121@stmail.ujs.edu.cn).

(*Corresponding Author*: *Li Quan*)

Digital Object Identifier 10.30941/CESTEMS.2025.00040

2096-3564 © 2025 CES

Therefore, addressing the practical application needs of electric vehicles, effectively suppressing electromagnetic vibration under flux-weakening operation while maintaining torque performance remains a significant challenge.

This paper proposes a method for suppressing electromagnetic vibration by designing ARM-MMF harmonic components from the perspective of the saliency ratio. The saliency ratio [13]-[14], as a key parameter of IPMSM, modulates the harmonic distribution of ARM-MMF through its numerical characteristics. By reasonably designing the saliency ratio, it is possible to effectively suppress the higher-order harmonic of ARM-MMF under flux-weakening operation, thereby suppressing REF. Section II analyzes the mechanism of vibration generation under flux-weakening operation and establishes a theoretical analysis model linking saliency ratio, ARM-MMF, and electromagnetic vibration, proposing the concept of achieving low-vibration design from the perspective of saliency ratio. In Section III, considering both high-speed vibration suppression and low-speed torque output design criteria, a rotor topology structure capable of dynamic saliency ratio adjustment is designed. Section IV conducts parameter design and performance analysis of the proposed motor structure, verifying the effectiveness of the proposed low-vibration motor design method. In Section V, a prototype motor is fabricated and experimentally validated. Finally, Section VI summarizes the paper.

II. Research on Vibration Characteristics under Flux-weakening Operation

In this section, a 36-slot/8-pole IPMSM is selected to study the vibration performance under flux-weakening speed extension, and the principles of vibration generation are analyzed.

A. Vibration Characteristics of Motors under Flux-weakening Speed Extension

Fig. 1 shows a two-dimensional model of a traditional PMSM for vehicles, which adopts a 36-slot/8-pole V-shaped interior permanent magnet structure. Fig. 1(b) shows the standard driving cycle — New European Driving Cycles (NEDC) operating conditions. It can be observed that the vehicle operating conditions are mainly divided into frequent start-stop, heavy-load climbing, road driving, and high-speed cruising. These correspond respectively to PM motor operating under low-speed high-torque, medium-speed light-load, and flux-weakening speed extension operation. To analyze the vibration characteristics of IPMSM under different operating conditions, Fig. 2 compares the vibration acceleration spectrum diagrams and equivalent radiated power (ERP) level waterfall diagrams of the motor under low-speed heavy-load and high-speed flux-weakening conditions. As shown in Fig. 2(a), compared with the rated operating condition, the motor exhibits significantly larger vibration acceleration amplitudes under flux-weakening speed extension. It is noteworthy that under high-speed flux-weakening conditions, the amplitude of the 9*f* vibration component, where *f* is electrical frequency is approximately 4 mm/s^2. However, since it is significantly lower than the main vibration peaks (such as 4*f*, 8*f*), with the amplitude at 8*f* being 82.6% larger than that at 9*f*, it was treated as a secondary factor in vibration characteristic analysis and not discussed in detail. Correspondingly, ERP level waterfall diagram in Figs. 2(b) and 2(c) demonstrate significantly elevated ERP levels under flux-weakening speed extension, with some frequency bands exceeding 100 dB, particularly at 4*f* and 8*f* components. This indicates that, compared to low-speed heavy loads, high-speed flux-weakening significantly worsens the vibration characteristics of motors. Therefore, it is necessary to implement vibration suppression for the motors under flux-weakening speed extension operation.

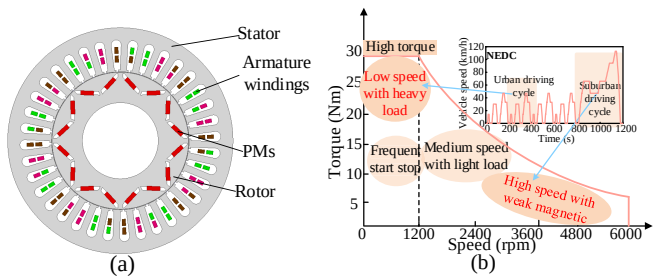

Fig. 1. Operating requirements for PM motors. (a) Structure field of 36-slot 8-pole interior permanent magnet (IPM) motor. (b) PM motor under variable operating conditions.

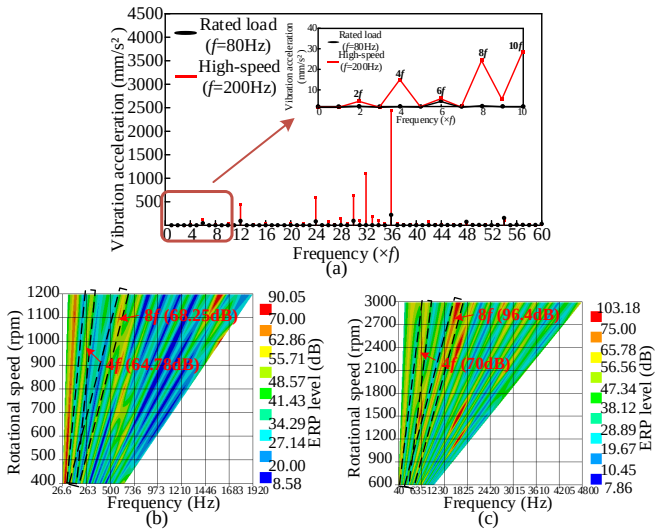

Fig. 2. Vibration performances. (a) Vibration acceleration. (b) ERP level waterfall diagram under rated operating conditions. (c) ERP level waterfall diagram under high-speed operating conditions.

B. Study on the Mechanism of Vibration Generation under Flux-weakening Operation

The electromagnetic vibration of IPMSM mainly originates from RER harmonics of the airgap magnetic field. This force acts on the stator core, causing radial deformation, which in turn triggers vibration and noise [15]. Therefore, in order to evaluate and suppress the electromagnetic vibration of the motor, the primary task is to study and analyze the characteristics of REF. According to Maxwell's tensor method, REF can be expressed as:

$$F_r(\theta,t)=\frac{B_r^2(\theta,t)-B_t^2(\theta,t)}{2\mu_0}\approx\frac{B_t^2(\theta,t)}{2\mu_0} \tag{1}$$

where $B_r(\theta, t)$ and $B_t(\theta, t)$ are the radial and tangential components of the airgap magnetic flux density, respectively; θ is the spatial angular position; t is the time; μ_0 is the magnetic permeability of free space.

From (1), it can be seen that the REF is positively correlated with the airgap magnetic flux density. Since the airgap magnetic field is composed of both the permanent magnet magnetic field and the armature magnetic field, the permanent magnet magnetomotive force (PM-MMF) and ARM-MMF can be expressed as:

$$\begin{aligned} f_{\mathrm{PM}}(\theta,t)&=\sum_{\mu=2m+1}F_\mu\cos\left(\mu_{\mathrm{p}}\theta-\mu\omega t\right)\\ f_{\mathrm{arm}}(\theta,t)&=\sum_{v=3n+1}F_v\cos\left(v_{\mathrm{a}}\theta-S_v\omega t\right)\end{aligned} \tag{2}$$

where F_μ and F_v are the amplitudes of the μth and vth PM-MMF harmonics and ARM-MMF harmonics, respectively; ω is the angular frequency of the current; μ_{p} is the harmonic order of PM-MMF; v_{a} is the harmonic order of ARM-MMF.

Therefore, substituting (2) into (1) yields:

$$\begin{aligned} F_r(\theta,t)&=\frac{\left(B_{\mathrm{PM}}+B_{\mathrm{arm}}\right)^2}{2\mu_0}\\ &=\frac{1}{2\mu_0}\left[f_{\mathrm{PM}}(\theta,t)\cdot\lambda+f_{\mathrm{arm}}(\theta,t)\cdot\lambda\right]^2\\ &=\frac{1}{2\mu_0}\left(\sum_\mu F_\mu\cos\left(\mu_{\mathrm{p}}\theta-\mu\omega t\right)\cdot\lambda+\right.\\ &\quad\left.\sum_v F_v\cos\left(v_{\mathrm{a}}\theta-S_v\omega t\right)\cdot\lambda\right)^2\end{aligned} \tag{3}$$

where B_{PM} is the permanent magnet field; B_{arm} is the armature magnetic field; λ is the airgap permeability.

Therefore, according to (3), the REF is generated by the interaction between ARM-MMF and PM-MMF. However, compared to PM-MMF, flux-weakening operation primarily alters the distribution of ARM-MMF. This leads to increased REF amplitudes, consequently causing aggravated vibrations during flux-weakening operation. Fig. 3 shows the three-dimensional (3-D) spatiotemporal distribution of ARM-MMF and REF. As shown in Fig. 3(a), when the motor operates under flux-weakening operation, although the fundamental component of ARM-MMF reduces, the amplitude of ARM-MMF harmonics that generate the lowest non-zero order REF actually increases, such as (8th, 11*f*), (12th, 3*f*), (16th, 1*f*), and (20th, 5*f*). Therefore, the amplitudes of the fourth-order REF such as 4*f* and 8*f* also increase, as shown in Fig. 3(b). This is the main reason for the intensification of vibration in flux-weakening operation.

C. Design Principle for Saliency Ratio under Flux-weakening Operation

To further investigate the impact of flux-weakening speed extension on the electromagnetic vibration of motors, it is necessary to study the underlying mechanism through which flux-weakening affects ARM-MMF. The principle of flux-

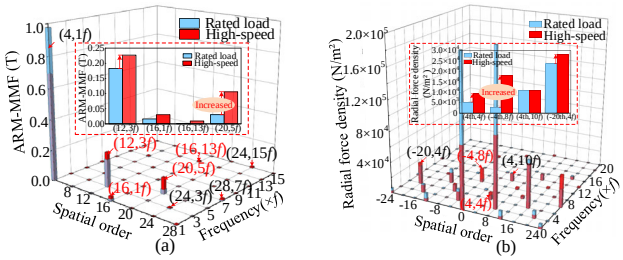

Fig. 3. The basic electromagnetic performance of IPMSM. (a) Spatial-temporal distribution of ARM-MMF. (b) Spatial-temporal distribution of REF.

weakening speed extension is to increase the d-axis current component and reduce the q-axis current component, thereby weakening the airgap magnetic field, allowing the motor speed to continue to increase steadily, and enabling the motor to operate at higher speeds.

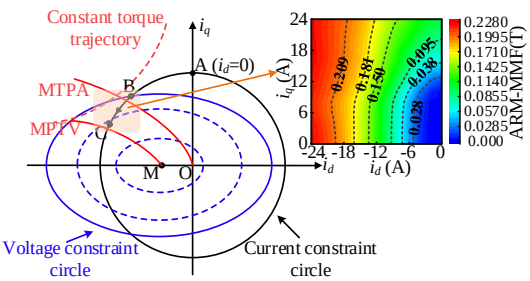

Fig. 4. Characteristics of current and voltage constraint circles.

Fig. 4 shows the motor current vector trajectory diagram and the relationship between ARM-MMF and the degree of flux-weakening. In the BC segment, the motor is in flux-weakening speed extension stage, and ARM-MMF increases with the degree of flux-weakening. At this point, the ARM-MMF can be further expressed as:

$$\begin{cases} f_{\mathrm{arm}}=f_{\mathrm{d,arm}}+f_{\mathrm{q,arm}}\\ f_{\mathrm{d,arm}}=\dfrac{B_{\mathrm{d,arm}}}{\lambda}=\dfrac{-L_{\mathrm{d}}i_{\mathrm{d}}}{\lambda NS}\\ f_{\mathrm{q,arm}}=\dfrac{B_{\mathrm{q,arm}}}{\lambda}=\dfrac{\alpha L_{\mathrm{q}}i_{\mathrm{q}}}{\lambda NS}\end{cases} \tag{4}$$

where f_{arm} is the ARM-MMF; $f_{\mathrm{d,arm}}$ is the d-axis ARM-MMF; $f_{\mathrm{q,arm}}$ is the q-axis ARM-MMF; $B_{\mathrm{d,arm}}$ is the d-axis armature magnetic field; $B_{\mathrm{q,arm}}$ is the q-axis armature magnetic field; L_{d} is the d-axis inductance; i_{d} is the d-axis current; L_{q} is the q-axis inductance; i_{q} is the q-axis current; α is the coupling coefficient; S is the effective area perpendicular to the magnetic field direction; N is the number of turns.

It can be observed that flux-weakening current and dq-axis inductance influence ARM-MMF. However, the regulation of armature current is constrained by multiple factors such as inverter capacity, temperature rise limits, and system efficiency, making it difficult to adjust specifically for vibration suppression requirements. Therefore, this paper investigates the intrinsic correlation mechanism between electromagnetic vibration and dq-axis inductance characteristics of the motor itself.

The inductance characteristics of IPMSM are generally L_{q} greater than L_{d}, and the saliency ratio is the ratio of the dq-

axis inductance. Therefore, a certain relationship has been found between the saliency ratio and ARM-MMF:

$$\begin{cases} K = \dfrac{L_q}{L_d} \\ f_{q,arm} = \dfrac{\alpha L_q i_q}{\lambda NS} = \dfrac{\alpha K L_d i_q}{\lambda NS} \end{cases} \tag{5}$$

where K is the saliency ratio.

Substituting (4) and (5) into (3) yields the relationship between the saliency ratio and REF as:

$$\begin{aligned} F_r &= \frac{1}{2\mu_0}\left(f_{pm}\cdot\lambda + f_{arm}\cdot\lambda \right)^2 \\ &= \frac{1}{2\mu_0}\left[f_{pm}\cdot\lambda + \frac{L_d\left(\alpha K i_q - i_d\right)}{NS} \right]^2 \end{aligned} \tag{6}$$

As shown in (4)-(6), the saliency ratio is a key factor in designing ARM-MMF and REF, and changes in its value directly affect the harmonic amplitude of ARM-MMF and REF.

Additionally, since the saliency ratio is closely related to torque, the effect of the saliency ratio on torque cannot be ignored when suppressing vibration noise through the saliency ratio.

$$T_e = \frac{3}{2} P_r \left[\psi_{PM} i_q + L_d \left(1 - K\right) i_d i_q \right] + T_{cog} \tag{7}$$

where P_r represents the number of pole pairs, and Ψ_{PM} represents the permanent magnet flux linkage.

The relationship between ARM-MMF and REF as a function of the saliency ratio is shown in Fig. 5. It can be seen that as the saliency ratio increases, the amplitude of the fundamental component in ARM-MMF continues to decrease, while the amplitudes of higher-order harmonics such as (8th, 11*f*) and (12th, 3*f*) show a significant increasing trend. The (20th, 5*f*) ARM-MMF harmonic exhibits a trend of first decreasing and then increasing. Correspondingly, the amplitude of REF harmonics (0th, 0*f*) and (8th, 2*f*) is negatively correlated with the saliency ratio, while the amplitude of REF harmonics (–4th, 2*f*) and (4th, 4*f*) increases with increasing K value. Among these, the amplitude of the (–4th, 8*f*) harmonic REF wave exhibits a trend of first decreasing and then increasing. This harmonic evolution pattern reveals a close relationship between the saliency ratio and the characteristics of electromagnetic force waves. Therefore, by designing the saliency ratio, the harmonic distribution of ARM-MMF can be effectively regulated under flux-weakening operation, thereby suppressing motor vibration caused by electromagnetic force waves.

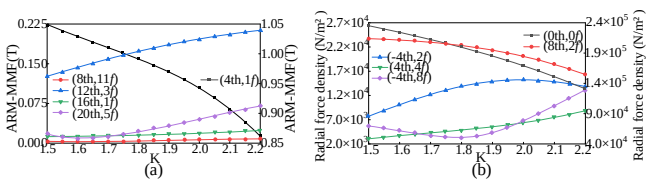

Fig. 5. Analysis of ARM-MMF and REF characteristics under variable saliency ratio. (a) ARM-MMF with the saliency ratio. (b) REF with the saliency ratio.

III. Permanent Magnet Motor Design Based on Saliency Ratio Design Method

The section employs saliency ratio design principles to optimize the spatial harmonic distribution of ARM-MMF through targeted dq-axis magnetic circuit modifications. The approach specifically suppresses critical ARM-MMF harmonics (8th, 11*f*), (12th, 3*f*), (16th, 1*f*), and (20th, 5*f*) order that excite dominant REF, such as (4th, 4*f*) and (–4th, 8*f*) order, during flux-weakening speed extension, thereby improving motor vibration performance.

A. Evolution of Motor Topology

The low vibration design flowchart based on the saliency ratio is shown in Fig. 6. Firstly, a theoretical model is established to clarify the influence mechanism of key harmonics on vibration. Then, the saliency ratio is defined as the key design variable for the harmonic distribution of ARM-MMF. Secondly, a rotor structure featuring a combination of composite magnetic barriers and arc-shaped PMs is designed, enabling dynamic control of saliency ratio. Subsequently, with the saliency ratio as the optimization objective, the response surface method (RSM) is combined with the multi-objective genetic algorithm (MOGA) for optimization. Finally, optimal parameters are determined based on the Pareto front, completing the entire design optimization process.

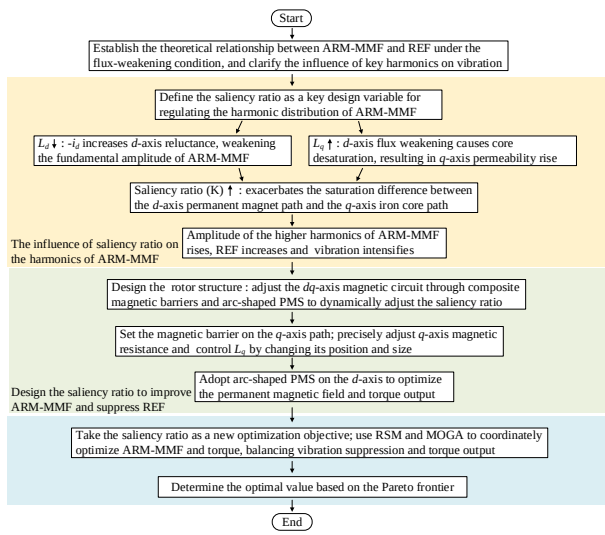

Fig. 6. Low vibration design flowchart based on saliency ratio.

The saliency ratio serves as a key parameter for characterizing the degree of difference in the dq-axis magnetic circuit inductance of an IPMSM, directly influencing the distribution characteristics of ARM-MMF harmonics [16]-[17]. When the motor is in a weak magnetic state, applying $-i_d$ to the d-axis magnetic circuit causes more magnetic flux to pass through the high-reluctance permanent magnet path, thereby reducing the d-axis inductance while weakening the fundamental amplitude of ARM-MMF. Meanwhile, under the influence of $-i_d$, the d-axis magnetic field weakens, reducing the core saturation state and increasing the magnetic permeability of the q-axis magnetic flux, thereby increasing

the q-axis inductance and saliency ratio. This further exacerbates the difference in saturation levels between the d-axis permanent magnet path and the q-axis core path. This enhanced non-uniformity in the magnetic permeability spatial distribution makes the modulation effect of magnetic permeability harmonics on ARM-MMF strength more pronounced, ultimately leading to an increase in the amplitude of higher-order harmonic magnetic flux.

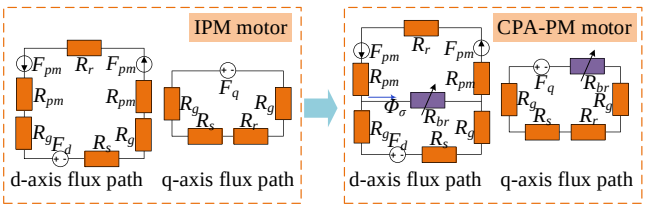

Fig. 7. Simplified equivalent magnetic circuit model.

To illustrate the principles of the saliency ratio design, the corresponding simplified equivalent magnetic circuit models for the d-axis and q-axis are shown in Fig. 7, where the magnetic circuit paths for the d-axis and q-axis are represented at different rotor positions. Compared to the magnetic circuit model of a traditional permanent magnet motor, this model introduces an additional variable resistor unit R_{br}. The characteristics of this unit change with variations in the armature current, thereby dynamically adjusting the saturation level of the magnetic circuit and influencing the dq-axis inductance values. Therefore, the variable resistor plays a crucial role in achieving dynamic leakage flux and saliency ratio. As shown in the figure, the dq-axis inductances and leakage flux can be expressed as:

$$\begin{cases} L_{\mathrm{d}} = \dfrac{N^2}{\left(2R_{\mathrm{pm}} + R_{\mathrm{r}} + R_{\mathrm{s}} + 2R_g\right)} \\ L_{\mathrm{q}} = \dfrac{N^2}{\left(R_{\mathrm{r}} + R_{\mathrm{s}} + 2R_g + R_{\mathrm{br}}\right)} \\ \phi_\sigma = \dfrac{F_{\mathrm{q}}}{\left(R_{\mathrm{r}} + R_{\mathrm{s}} + 2R_g + R_{\mathrm{br}}\right)} \\ K = \dfrac{L_{\mathrm{q}}}{L_{\mathrm{d}}} = \dfrac{\phi_\sigma \times \left(2R_{\mathrm{pm}} + R_{\mathrm{r}} + R_{\mathrm{s}} + 2R_g\right)}{F_{\mathrm{q}}} \end{cases} \tag{8}$$

where R_{pm} is the permanent magnet reluctance; R_{g} is the air gap reluctance; R_{r} is the rotor core reluctance; R_{s} is the stator core reluctance; R_{br} is the variable reluctance; F_{q} is the q-axis MMF.

Based on the above theoretical analysis, a convex pole adjustable permanent magnet (CPA-PM) motor is proposed. Fig. 8 shows the evolution of the rotor topology from traditional IPM motor to CPA-PM motor, with a focus on improving the permanent magnet layout and magnetic barrier structure design. The motor adopts a composite magnetic barrier structure that integrates elliptical and arc-shaped in the rotor q-axis magnetic circuit. This configuration creates a variable leakage magnetic path and achieves variable magnetic resistance. Compared to traditional V-shaped permanent magnet motors, this structure not only enables precise control over the q-axis magnetic circuit but also demonstrates significant advantages in enhancing the saliency ratio and optimizing magnetic field distribution. The design of two sets of three-segment arc-shaped magnetic barriers, which prevent the q-axis magnetic field from saturating, reduce the q-axis magnetic resistance, and increase the q-axis inductance. Additionally, the multi-layer magnetic barrier structure improves the path of the q-axis magnetic flux, effectively suppressing magnetic flux leakage. On the d-axis magnetic circuit, arc-shaped PM are used instead of V-shaped PM, effectively improving PM utilization and enhancing torque output capability. Combined with the magnetic barrier design, this reduces magnetic leakage while enhancing d-axis magnetic field saturation, thereby achieving reduced d-axis inductance. The motor achieves flexible adjustment of the saliency ratio through the rotor magnetic circuit design. The unique arc-shaped magnetic barrier structure regulates the dq-axis inductance interaction by guiding the main magnetic flux leakage, thereby reducing the saliency ratio and suppressing the harmonics of ARM-MMF (8th, 11*f*) and (12th, 3*f*), achieving targeted suppression of REF.

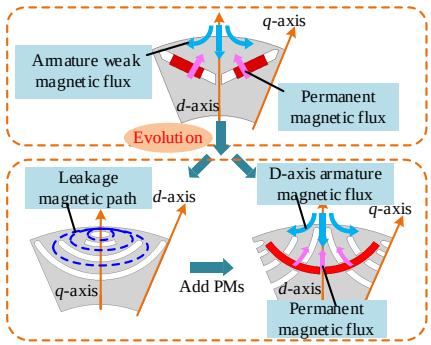

Fig. 8. Rotor evolution from the conventional IPM motor to the CPA-PM motor.

The cloud diagram of the ARM-MMF harmonics (8th, 11*f*) and (12th, 3*f*) of a CPA-PM motor as a function of the saliency ratio are shown in Fig. 9, with the horizontal and vertical axis representing the dq-axis inductance. ARM-MMF harmonic components generally exhibit a decreasing trend as the saliency ratio decreases, verifying the feasibility of the saliency ratio design. The motor proposed in this study is illustrated in Fig. 10, and the basic design requirements are listed in Table I. CPA-PM motor was configured with a higher current setting. The core reason for this was to adapt to its unique magnetic circuit structure, ensuring that the internal magnetic field and output torque of the motor reached levels comparable to those of traditional motors. This design aimed to establish a fair comparison of their output capabilities.

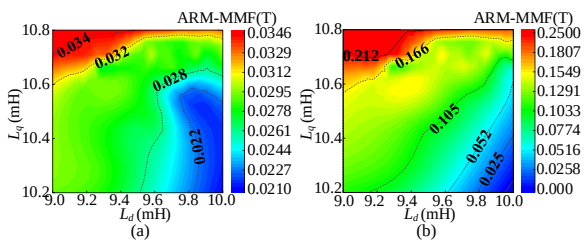

Fig. 9. Cloud diagram of ARM-MMF harmonics with saliency ratio. (a) (8th, 11*f*)-order ARM-MMF. (b) (12th, 3*f*)-order ARM-MMF.

B. Performance Verification

To validate the effectiveness of the proposed motor saliency ratio design method, the performance of IPMSM motor and CPA-PM motor is analyzed and verified.

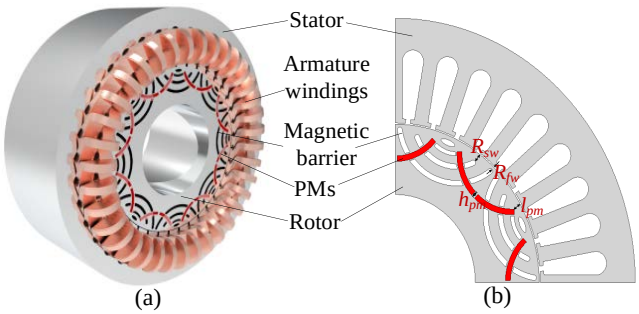

Fig. 10. Proposed CPA-PM motor. (a) Configuration. (b) Parametric geometric structure of motor.

TABLE I
BASIC DESIGN SPECIFICATIONS AND PARAMETERS

Items	IPM motor	CPA-PM motor
Rated output power/kW	4	4
Rated speed/(r/min)	1200	1200
Phase rated current/A	18	21
Stack length/mm	65	65
Air gap length/mm	0.5	0.5
Stator outer radius/mm	95	95
Rotor outer radius/mm	57.5	57.5
Rotor inner radius/mm	32	32

Fig. 11 shows the three-dimensional spatiotemporal distribution of ARM-MMF and REF. Except for the fundamental wave, the amplitudes of other harmonic orders of ARM-MMF decrease to varying degrees. Furthermore, the fourth-order harmonics such as 4*f* and 8*f*, which are generated by the interaction between ARM-MMF harmonics (8th, 11*f*), (12th, 3*f*), (16th, 1*f*), (16th, 13*f*) and (20th, 5*f*), are significantly attenuated.

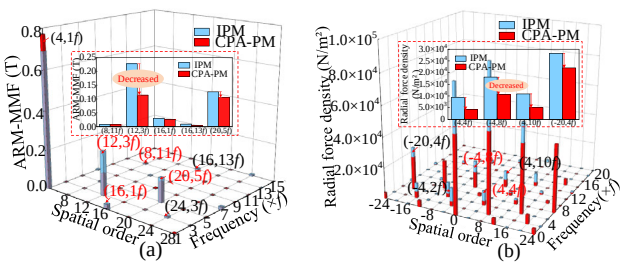

Fig. 11. Spatial-temporal distribution of ARM-MMF and REF. (a) ARM-MMF. (b) REF.

The above results indicate that by regulating the saliency ratio, ARM-MMF of the motor was successfully suppressed, thereby suppressing the harmonic amplitude of REF. The torque and vibration acceleration diagrams of the designed motor are shown in Fig. 12. The proposed motor achieves a marginal torque improvement while reducing torque ripple by approximately 7%. The vibration acceleration at 4*f* and 8*f* is lower than that of the traditional motor. Overall, the CPA-PM motor demonstrates significant advantages in vibration performance.

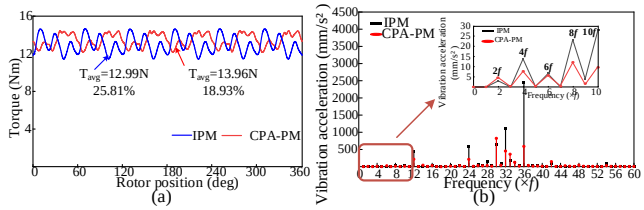

Fig. 12. Electromagnetic and mechanical coupling performance. (a) Torque. (b) Vibration acceleration.

IV. PARAMETER DESIGN AND PERFORMANCE EVALUATION

A. Harmonic-orientated Parameter Design

Based on the in-depth analysis of the electromagnetic vibration characteristics of CPA-PM motors discussed earlier, this study proposes a multi-parameter collaborative optimization design method aimed at further suppressing REF harmonics. As shown in the parameter schematic diagram in Fig. 10, this scheme focuses on four key design parameters: magnetic barrier position parameters (R_{sw}, R_{fw}), which are used to regulate the q-axis inductance characteristics; permanent magnet parameters (h_{pm}, l_{pm}), which regulate the d-axis inductance characteristics while ensuring the use of permanent magnets; the two parameters together determine the key parameters of the saliency ratio ($K = L_q/L_d$).

When establishing the optimization scheme, the objective function simultaneously considers minimizing the harmonic components of ARM-MMF that generates the critical REF and maximizing the output torque, ensuring both performances are optimized. At the same time, the saliency ratio is taken as the optimization target. Second, a MOGA is employed to obtain a Pareto front representing the trade-off relationships among objectives, rather than a single solution. Finally, torque constraints are set to ensure basic electric vehicle drive requirements are met, while an upper limit is imposed on REF to achieve low-vibration performance. Ultimately, through this constrained multi-objective co-optimization framework, we selected a design point from the Pareto front that achieves the optimal trade-off between vibration suppression and torque output. This comprehensive optimization method, which considers multiple parameters and objectives, balances the requirements for electromagnetic vibration suppression with torque performance requirements.

The optimization range for each parameter is determined comprehensively based on electromagnetic performance, mechanical reliability, and manufacturing feasibility [18]. Excessively small magnetic barrier value results in excessive proximity to the air gap, leading to reduced torque, insufficient mechanical strength of the magnetic bridge, and manufacturing difficulties. Excessively large values cause the magnetic barriers to be embedded too deeply into the rotor, weakening their ability to regulate the q-axis magnetic circuit, saturating the saliency ratio, and exacerbating vibration. As shown in Fig. 13, when parameters are excessively large, the saliency ratio increases significantly while the amplitude of REF harmonic (−4th, 8*f*) exceeds 10,000 N/m², severely

compromising vibration suppression performance. The parameter ranges described were determined through extensive simulation iterations to achieve an optimal balance between torque output, vibration suppression, and manufacturability. The final optimized ranges for each parameter are presented in Table II.

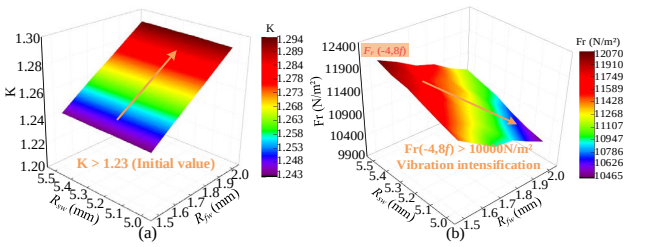

Fig. 13. Variation relationships of key parameters on leading harmonics (R_{fw} > 1.5 mm, R_{sw} > 5mm). (a) *K*. (b) (−4th, 8*f*)-order radial force.

TABLE II
VARIATION RANGE OF DESIGN VARIABLES

Parameters	Value range
End depth of the first magnetic barrier, R_{fw}/mm	[0.5–1.5]
End depth of the second magnetic barrier, R_{sw}/mm	[2.0–5.0]
Permanent magnet thickness, h_{pm}/mm	[1.5–2.5]
End depth of permanent magnet, l_{pm}/mm	[2.4–3.2]

Constraint boundary setting in multi-objective optimization balances driving performance and vibration suppression. The torque lower limit, based on vehicle requirements, is slightly higher than that of conventional motors to ensure power delivery under high-speed flux-weakening conditions while reserving optimization margin. (4th, 4*f*) and (−4th, 8*f*) of REF constraints are defined based on initial simulation amplitudes of 4263 and 10,672 N/m^2. By setting upper limits below initial values, the optimization direction is forced toward vibration suppression objectives. All constraints reference the initial model. The objective function and constraint conditions are as follows:

$$\begin{cases} \text{Function}: \left[\text{Min}\ \delta_1(K), \text{Min}\ \delta_2\left(f_{(4\text{th},4f)}\right), \right. \\ \left. \text{Min}\ \delta_3\left(f_{(-4\text{th},8f)}\right), \text{Max}\ \delta_4\left(T_{\text{out}}\right)\right] \\ \text{Constraints}: T_{\text{out}} > 13\text{N}\cdot\text{m}, \\ F_{(4\text{th},4f)} < 4.2\times10^3\ \text{N/m}^2, \\ F_{(-4\text{th},8f)} < 1.1\times10^4\ \text{N/m}^2 \end{cases} \tag{9}$$

where T_{out} is the output torque.

The response surface method was employed to analyze the effects of these parameters on the saliency ratio and harmonic components of ARM-MMF. As shown in Fig. 14, when the saliency ratio decreases, the harmonics of ARM-MMF, such as (8th, 11*f*) and (12th, 3*f*), are suppressed.

Furthermore, REF harmonic and torque response surface diagrams under parameter design are shown in Fig. 15. The main-order harmonics (4th, 4*f*) and (−4th, 8*f*) of REF generated by the interaction of ARM-MMF have been effectively suppressed. Additionally, the torque variation range, which serves as a constraint condition, is only 1 N·m. This saliency ratio-torque co-optimization based parameter design method achieves optimal balance between vibration suppression and torque output performance.

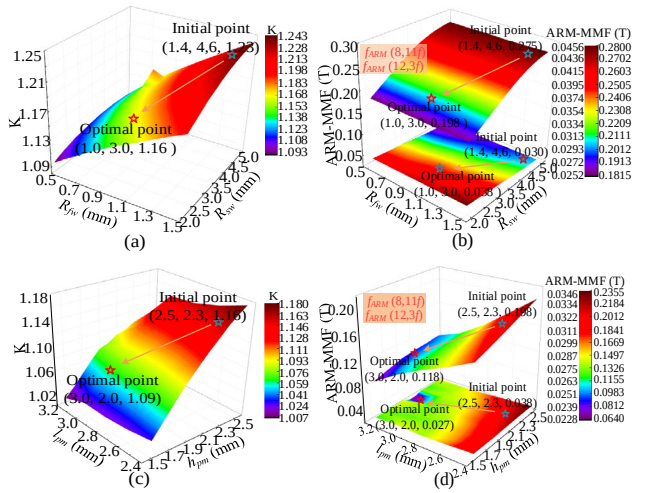

Fig. 14. Variation relationships of key parameters on leading harmonics. (a) *K* between R_{fw} and R_{sw}. (b) ARM-MMF between R_{fw} and R_{sw}. (c) *K* between l_{pm} and h_{pm}. (d) ARM-MMF between l_{pm} and h_{pm}.

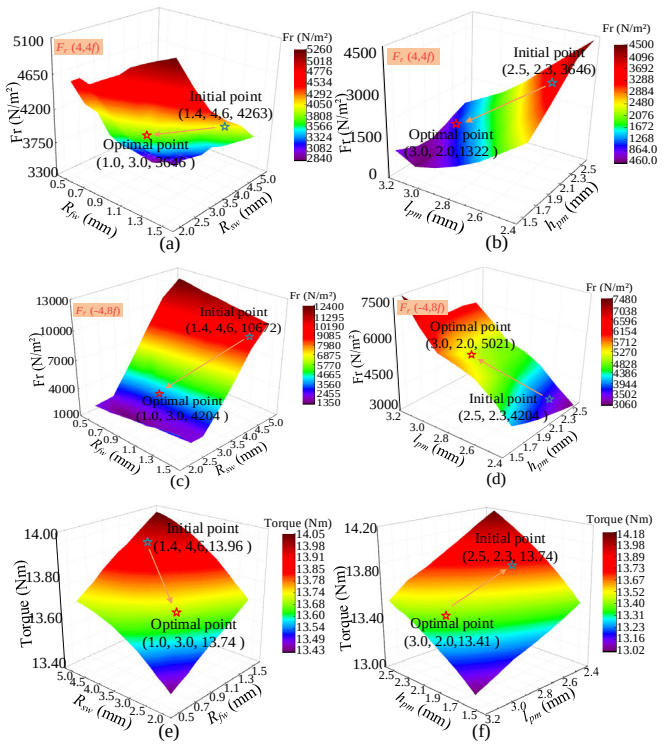

Fig. 15. Variation relationships of key parameters on leading harmonics. (a) (4th, 4*f*)-order radial force between R_{fw} and R_{sw}. (b) (4th, 4*f*)-order radial force between l_{pm} and h_{pm}. (c) (−4th, 8*f*)-order radial force between R_{fw} and R_{sw}. (d) (−4th, 8*f*)-order radial force between l_{pm} and h_{pm}. (e) Torque between R_{fw} and R_{sw}. (f) Torque between l_{pm} and h_{pm}.

Finally, to identify the optimal design for the CPA-PM motor, a MOGA is employed to determine optimal parameters. Fig. 16(a) shows the scatter plots of optimization objectives. As can be seen, optimization objectives converge to the Pareto front successfully. To facilitate visualization of the optimization objectives, parallel coordinate plots are utilized, as shown in Fig. 16(b). The optimal design point is

identified and marked in red within the diagram. The final optimized parameter values are summarized in Table III.

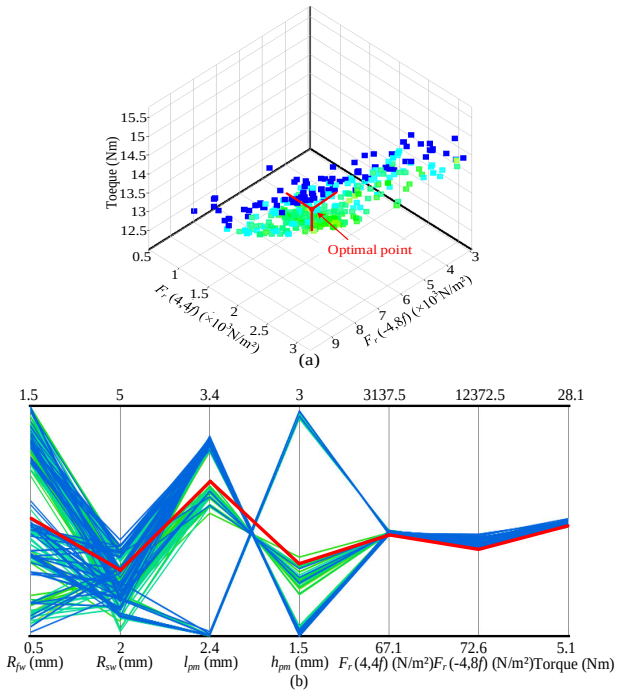

Fig. 16. Pareto front plot. (a) Pareto front of the MOGA. (b) Parallel coordinates plots of optimization objectives.

TABLE III
MOTOR SIZE AFTER OPTIMIZATION

Objective	Initial/mm	Optimal/mm	Objective	Initial/mm	Optimal/mm
R_{fw}	1.4	1	h_{pm}	2.3	2
R_{sw}	4.6	3	l_{pm}	2.5	3

B. *Performance Evaluation*

To verify the effectiveness of the CPA-PM motor and its optimization method, a detailed study of the electromagnetic performance of the CPA-PM motor was conducted using the finite element method.

First, the no-load back electromotive force (EMF) and torque of the initial and optimized CPA-PM motors at a speed of 1200 r/min were simulated, as shown in Fig. 17. As can be seen from Fig. 17(a), the optimized no-load back EMF waveform is more sinusoidal, and the amplitude has also increased. Additionally, a Fast Fourier Transform (FFT) analysis was performed on the simulated back EMF waveforms, yielding total harmonic distortion (THD) values of 7.15% and 5.4% for the initial and optimized motors, respectively, indicating that the optimized motor exhibits reduced torque ripple. Figs. 17(c) and 17(d) show the 3-D spatiotemporal distribution of ARM-MMF and REF, respectively. Compared to the initial motor, the optimal motor maintains the fundamental wave unchanged, while the harmonic components of ARM-MMF, such as (8th, 11*f*), (12th, 3*f*), (16th, 1*f*) and (20th, 5*f*), are reduced. The amplitude of the main-order REF harmonics generated by the interaction of ARM-MMF harmonics, such as (4th, 4*f*) and (−4th, 8*f*), also decreases accordingly.

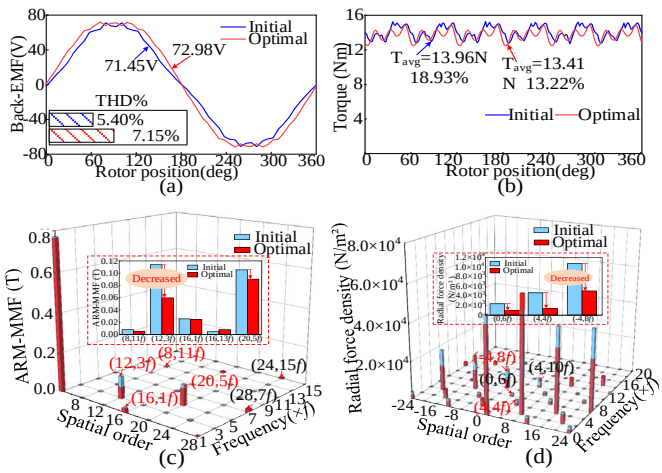

Fig. 17. Electromagnetic performances. (a) Back-EMF. (b) Torque. (c) ARM-MMF. (d) REF.

Fig. 18 shows the vibration acceleration of the CPA-PM motor. Within the 2000 Hz range, there are some areas with relatively large vibration acceleration amplitudes, such as 800 and 1600 Hz, which are consistent with the frequencies of 4*f* and 8*f* (*f* = 200 Hz) of REF. After optimization, the vibration acceleration amplitudes of 4*f* and 8*f* are further decreased. Additionally, Figs. 19 and 20 show the vibration displacement diagrams and ERP level waterfall diagram before and after optimization, respectively. The vibration performance of the CPA-PM motor is significantly improved after optimization. The vibration displacement amplitude at 4*f* decreased from

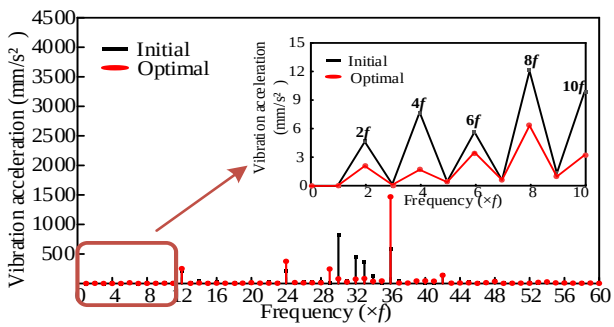

Fig. 18. Vibration acceleration.

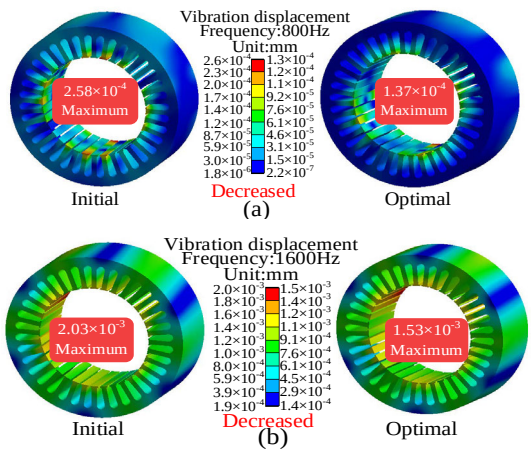

Fig. 19. Vibration performances. (a) Vibration displacement diagram of the motor under 800 Hz frequency. (b) Vibration displacement diagram of the motor under 1600 Hz frequency.

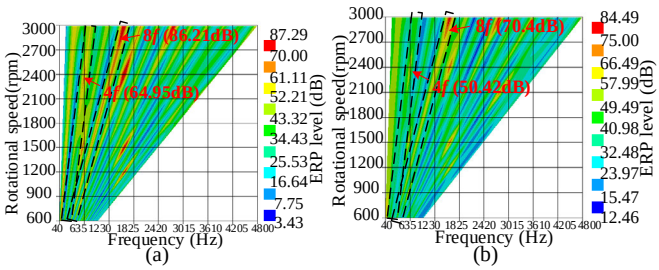

Fig. 20. Vibration performances. (a) ERP level waterfall diagram before optimization. (b) ERP level waterfall diagram after optimization.

0.258 μm in the initial design to 0.137 μm, and the vibration displacement amplitude at 8*f* decreased from 2.03 to 1.53 μm. Further analysis of the ERP level waterfall diagram shows that the noise amplitudes at 4*f* and 8*f* decreased by 14.53 and 15.81 dB, respectively, after optimization. This indicates that the motor vibration has been reduced after optimization.

V. Experiment Validation

To verify the correctness of the theoretical analysis, a CPA-PM motor was manufactured based on the optimization results. Fig. 21 shows the corresponding silicon steel sheets, the assembled motor, and the experimental platform. A high-performance drive controller, dSPACE 1103, was used to control the armature current. The experimental section used an inverter to supply power to and control the CPA-PM motor. Despite the complexity of its mold design and stamping process, the rotor of CPA-PM motor can be manufactured with conventional stamping technology, which enables mass production potential and cost benefits [13].

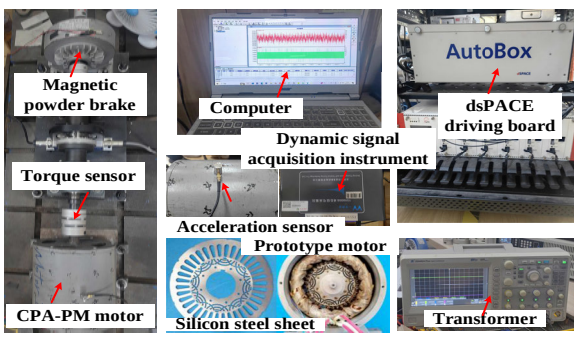

Fig. 21. Schematic diagram of the experimental platform.

Some basic experiments were conducted on the CPA-PM motor. First, Fig. 22 shows the three-phase no-load back EMF waveform measured at a rated speed of 1200 r/min. It can be seen that the measured back EMF waveform trend is consistent with the simulation results in Fig. 17, exhibiting sinusoidal and symmetrical characteristics.

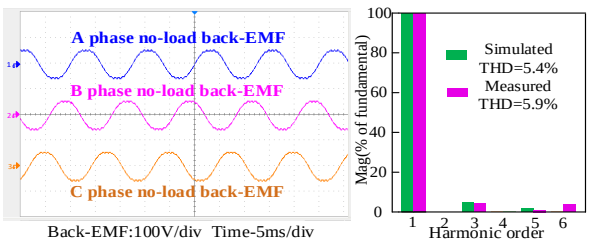

Fig. 22. No-load back EMF performance.

Fig. 23 displays steady-state torque waveforms and motor dynamic characteristics. Fig. 23(a) shows the steady-state torque waveform at i_d = 0. It can be observed that the measured output torque is slightly lower than the simulated value, primarily due to manufacturing tolerances in the motor. In Fig. 23(b), it can be observed that the current is 20 A at this time, and $-i_d$ has been applied to put the motor into flux-weakening state. In Fig. 23(c), the motor is given a torque of 5 N·m, and the speed rises steadily at a speed of 200 r/min, indicating that the motor has good speed dynamic response.

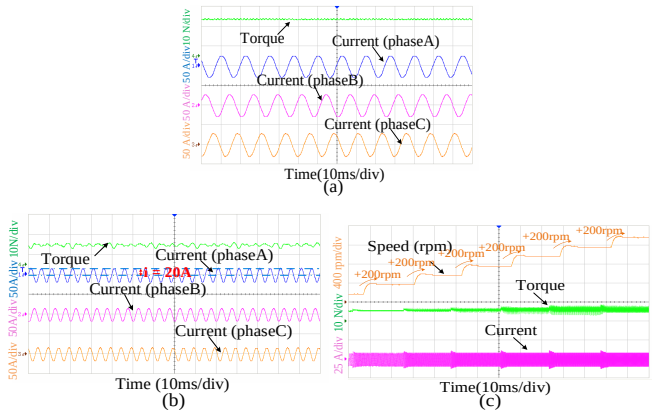

Fig. 23. Steady torque and variable speed experiment. (a) Steady torque and current waveforms of the motor (i_d = 0). (b) Steady torque and current waveforms of the motor (i_d < 0). (c) Variable speed experiment of the proposed motor.

Fig. 24 shows the vibration acceleration waveforms of the CPA-PM motor under rated load and high-speed flux-weakening operation. There are several significant vibration points in the low-frequency range, corresponding to frequencies that are even multiples of the fundamental frequency *f*, such as 2*f*, 4*f*, 6*f*, 8*f* and 10*f*, consistent with theoretical analysis. Under flux-weakening operation, the peak acceleration amplitudes occur at 4*f* and 8*f*, which is consistent with simulation results, thus verifying the effectiveness of the low-vibration design and analysis of the CPA-PM motor. The 3-D frequency spectrum and waterfall plot of vibration acceleration are shown in Fig. 25. The major vibrations primarily occur in the 0-2000 Hz range, primarily due to the relatively large amplitudes of low-frequency REF at frequencies such as 4*f* and 8*f*.

Overall, a certain deviation exists between the electromagnetic characteristic simulations and experiments, primarily stemming from limitations of the experimental system. Accelerometers exhibit an inherent measurement error of approximately 3%, while insufficient mounting surface flatness introduces mechanical vibration background noise. Additionally, controller delays cause the actual current harmonic content to increase compared to the simulation. Despite these systematic deviations, the overall trends between experimental results and simulation predictions remain consistent. The distribution characteristics of key vibration orders are highly consistent with the simulated spectrum. Furthermore, the CPA-PM motor demonstrates significantly enhanced vibration suppression compared to conventional motors, fully validating the correctness and

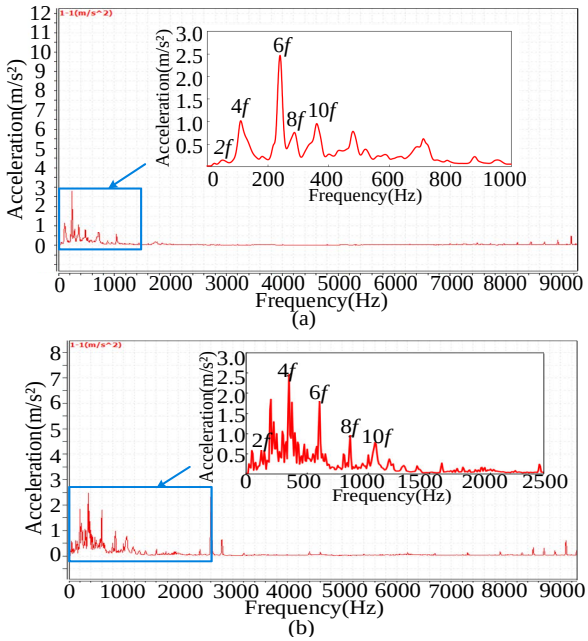

Fig. 24. Vibration acceleration test of CPA-PM motor. (a) Vibration acceleration under rated operating conditions. (b) Vibration acceleration under high-speed flux-weakening operating conditions.

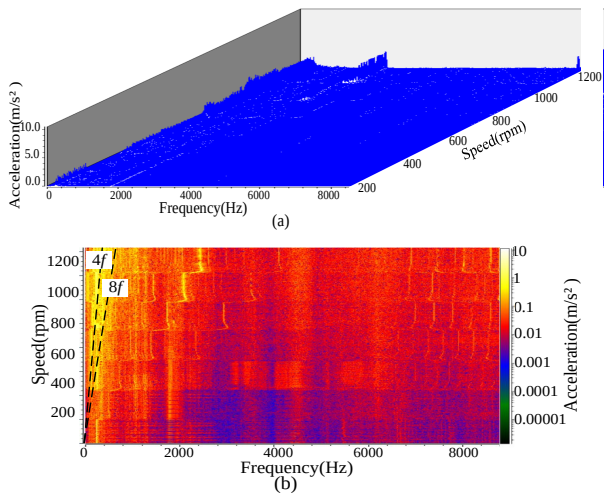

Fig. 25. Variable Vibration results of CPA-PM motor. (a) 3-D frequency spectra. (b) Waterfall plot.

effectiveness of the theoretical model and optimization method presented in this paper.

VI. Conclusion

In this paper, a radial electromagnetic force harmonic design method from the perspective of saliency ratio was proposed, achieving low-vibration design for IPMSM. First, a theoretical model for vibration analysis under flux-weakening operation was established, revealing the mechanism behind vibration amplification during flux-weakening speed extension. This phenomenon was triggered by enhanced high-order harmonics in ARM-MMF, which increase the wave amplitude of REF. Then, by analyzing the intrinsic mechanism between saliency rate, ARM-MMF, and REF, a method for suppressing key ARM-MMF harmonics through saliency ratio regulation was proposed. Based on this, a CPA-PM motor topology was designed. Additionally, a saliency ratio-torque co-optimization methodology was proposed, which achieved simultaneous reduction of dominant vibration component 4*f* and 8*f* by 68.9% and 52.9% respectively while maintaining superior torque performance. The effectiveness of this design method was ultimately validated through simulation and experimentation.

References

[1] Y. Kong, M. Y. Lin, and L. Jia, "A Novel High Power Density Permanent-magnet Synchronous Machine with Wide Speed Range," *IEEE Trans. on Magn.*, vol. 56, no. 2, pp. 1–6, Feb. 2020.

[2] Z. X. Xiang, J. Q. Wei, and X. Y. Zhu, "Torque Ripple Suppression of a PM Vernier Machine from Perspective of Time and Space Harmonic Magnetic Field," *IEEE Trans. on Ind. Electron.*, vol. 71, no. 9, pp. 10150–10161, Sept. 2024.

[3] D. E. Pinto, A. -C. Pop, and G. Myrria *et al.*, "Vibration Analysis of Delta-connected PMSMs Using Lookup Table-based Models—Influence of the 0-sequence Component," *IEEE Trans. on Ind. Electron.*, vol. 69, no. 7, pp. 6561–6571, Jul. 2022.

[4] J. B. Zou, M. C. Liu, and Y. X. Xu *et al.*, "Vibration Contribution Analysis of Radial and Tangential Electromagnetic Force Harmonic of Permanent Magnet Synchronous Motor," *IEEE Trans. on Appl. Supercon.*, vol. 34, no. 8, pp. 1–5, Nov. 2024.

[5] W. J. Fan, X. Y. Zhu, and L. Quan *et al.*, "Flux-weakening Capability Enhancement Design and Optimization of a Controllable Leakage Flux Multilayer Barrier PM Motor," *IEEE Trans. on Ind. Electron.*, vol. 68, no. 9, pp. 7814–7825, Sept. 2021.

[6] S. M. Wang, J. F. Hong, and Y. G. Sun *et al.*, "Effect Comparison of Zigzag Skew PM Pole and Straight Skew Slot for Vibration Mitigation of PM Brush DC Motors," *IEEE Trans. on Ind. Electron.*, vol. 67, no. 6, pp. 4752–4761, Jun. 2020.

[7] C. Peng, D. H. Wang, and B. D. Wang *et al.*, "Different Rotor Segmented Approaches for Electromagnetic Vibration and Acoustic Noise Mitigation in Permanent Magnet Drive Motor: A Comparative Study," *IEEE Trans. on Ind. Electron.*, vol. 71, no. 2, pp. 1223–1233, Feb. 2024.

[8] O. Gundogmus, S. Das, and Y. Yasa *et al.*, "Acoustic Noise Mitigation in High Pole Count Switched Reluctance Machines Utilizing Skewing Method on Stator and Rotor Poles," *IEEE Trans. on Ind. Electron.*, vol. 69, no. 6, pp. 5581–5593, Jun. 2022.

[9] B. D. Wang, D. H. Wang, and J. Nie *et al.*, "Zero-order Electromagnetic Vibration Suppression of Permanent Magnet Synchronous Motor with Harmonic Currents Injection," *IEEE Trans. on Magn.*, vol. 61, no. 2, pp. 1–5, Feb. 2025.

[10] Y. D. Guo, K. Wang, and H. Y. Sun, "Influence of Magnet Field Harmonics on Radial Force of Fractional-slot PM Machines Considering Slot/Pole Combinations," *IEEE Trans. on Magn.*, vol. 59, no. 11, pp. 1–6, Nov. 2023.

[11] T. Liu, L. Quan, and D. Y. Fan *et al.*, "Low Vibration Research and Design of In-wheel V-shaped PM Motor from the Perspective of Winding Magnetomotive Force," *IEEE Trans. on Magn.*, vol. 60, no. 9, pp. 1–7, Sept. 2024.

[12] S. H. Zhao, J. H. Chen, and C. Zhang *et al.*, "Low-frequency Electromagnetic Vibration of DTP-PMSM Considering Current Harmonics and Winding Operating Modes," *IEEE Trans. on Ind. Appl.*, vol. 61, no. 2, pp. 3016–3025, Mar.-Apr. 2025.

[13] X. Zhou, X. Y. Zhu, and W. Y. Wu *et al.*, "Multi-objective Optimization Design of Variable-saliency-ratio PM Motor Considering Driving Cycles," *IEEE Trans. on Ind. Electron.*, vol. 68, no. 8, pp. 6516–6526, Aug. 2021.

[14] W. Liu, H. Yang, and H. Y. Lin *et al.*, "Design Tradeoff Between Saliency Ratio and PM Flux Linkage in Variable Flux Memory Machines," *IEEE Trans. on Energy Convers.*, vol. 38, no. 1, pp. 562–572, Mar. 2023.

[15] W. Y. Liang, J. F. Wang, and P. C. -K. Luk *et al*., "Analytical Study of Stator Tooth Modulation on Electromagnetic Radial Force in Permanent Magnet Synchronous Machines," *IEEE Trans. on Ind. Electron.*, vol. 68, no. 12, pp. 11731–11739, Dec. 2021.

[16] X. X. Rao, L. Rong, and W. S. Gan *et al*., "Investigation of Noise Sources in Fractional-slot Concentrated Winding Motors Considering High-order Radial/Tangential Electromagnetic Force Combination and Modulation," *IEEE Access*, vol. 11, pp. 143980–143997, 2023.

[17] L. Xu, X. Y. Zhu, and W. Y. Wu *et al*., "Flux-leakage Design Principle and Multiple-operating Conditions Modeling of Flux Leakage Controllable PM Machine Considering Driving Cycles," *IEEE Trans. on Ind. Electron*., vol. 69, no. 9, pp. 8862–8874, Sept. 2022.

[18] Z. X. Xiang, Y. T. Zhou, and X. Y. Zhu *et al*., "Research on Characteristic Airgap Harmonics of a Double-rotor Flux-modulated PM Motor Based on Harmonic Dimensionality Reduction," *IEEE Trans. on Transp. Electrif*., vol. 10, no. 3, pp. 5750–5761, Sept. 2024.

Hui Qu received the B.Sc. degree in automation from Jinling Institute of Technology, Nanjing, China, in 2023. She is currently working toward the M.Sc degree in control engineering with Jiangsu University, Zhenjiang, China.

Her research interests include design and vibration performance analysis of hairpin winding motors for electric vehicles.

Li Quan received the B.Sc. degree in electrical engineering from the Hefei University of Technology, Hefei, China, in 1985, the M.Sc. degree in motors and electrical specialty from Southeast University, Nanjing, China, in 1991, and the Ph.D. degree in power electronics and power transmission from the Nanjing University of Aeronautics and Astronautics, Nanjing, in 2007.

Since 1998, he has been with Jiangsu University, Zhenjiang, China, where he is currently a professor with the School of Electrical and Information Engineering. He has authored or coauthored more than 100 technical papers, one textbook, and holds three patents in these areas. His teaching and research interests include high performance permanent magnet motor for electric vehicles, double rotor permanent magnet motor for hybrid electric vehicles, and motor drives control.

Xiaoyong Zhu (Member, IEEE) received the B.Sc. and M.Sc. degrees in electrical engineering from Jiangsu University, Zhenjiang, China, in 1997 and 2002, respectively, and the Ph.D. degree in electrical machinery and appliances from the School of Electrical Engineering, Southeast University, Nanjing, China, in 2008. During the period of doctoral study, his subject was electrical engineering, mainly focused on the design, analysis, and control of the type of hybrid-excited permanent magnet machine.

Since 1999, he has been with Jiangsu University, where he is currently a professor with the School of Electrical Information Engineering. From 2007 to 2008, he was a research assistant with the Department of Electrical and Electronic Engineering, University of Hong Kong, Hong Kong, China. From 2012 to 2013, he was a visiting professor with the Department of Energy-Funded Graduate Automotive Technology Education Center for Electric Drive Transportation, University of Michigan, Dearborn, Michigan, USA. He has authored or coauthored more than 70 referred technical papers, and holds 12 patents on the topics of his research interests, which include design and drive control of electric machines with wide-speed range, less rare-earth permanent magnet motor, and multiport permanent magnet motor.

Zixuan Xiang (Member, IEEE) received the B.Sc. degree in electrical engineering and automation from Hubei Polytechnic University, Huangshi, China, in 2010, and the Ph.D degree in power electronics and power transmission from the School of Electrical and Information Engineering, Jiangsu University, Zhenjiang, China, in 2017, respectively.

He is currently an associate professor with the School of Electrical and Information Engineering, Jiangsu University. His main research interests include design, optimization, and drive control of high performance permanent magnet motor and novel double mechanical port permanent magnet motor for application in modern electric vehicles and hybrid electric vehicles.

Teng Liu received the B.Sc. degree in electrical engineering and automation from Jiangsu University, Zhenjiang, China, in 2021, where he is currently working toward the Ph.D. degree in electrical engineering.

His current research interests include design and analysis of permanent magnet motors with low speed and high torque output, and with vibration and acoustic noise.

Jiamin Bai received the B.Sc. degree in electrical engineering and automation from University of Shanghai for Science and Technology, Shanghai, China, in 2021, where she is currently working towards the Ph.D degree in electrical engineering.

Her current research interests include design and optimization of permanent magnet machine for application in modern electric vehicles and hybrid electric vehicles.